Physics-informed machine learning and mechanistic modeling of additive manufacturing to reduce defects

Y. Du, T. Mukherjee, T. DebRoy*

Department of Materials Science and Engineering, The Pennsylvania State University, University Park, PA 16802, USA

A R T I C L E   I N F O

A B S T R A C T

In the past few decades, additive manufacturing has evolved for the one-step fabrication of various complex, customized metallic components that cannot be easily and economically produced by other means. However, widespread applications and market penetration of such components are often hindered by the formation of common defects that affect part quality, reliability, and serviceability, and increase the cost. Here, for the first time, we show that a combination of physics-informed machine learning, mechanistic modeling, and experimental data can reduce the occurrence of common defects in additive manufacturing. By analyzing experimental data on the defect formation for commonly used alloys available in the disjointed, peer-reviewed literature, we identify several important variables that reveal the physics behind the defect formation. Values of those variables computed using a mechanistic model, when used in a physics-informed machine learning, provide the hierarchical importance of the variables on defect formation. In addition, based on the results of the physics-informed machine learning, we provide easy-to-use, verifiable, quantitative formalism that can be used in real-time to predict defects before experiments. The proposed methodology can help in reducing common defects such as balling, cracking, lack of fusion, porosity, and surface roughness, and solve other complex engineering problems beyond additive manufacturing.

1. Introduction

Additive manufacturing (AM) of metallic materials is a rapidly progressing field because of its capability to fabricate complex, and intricate components easily and economically for aerospace, consumer products, healthcare, energy, automotive, and marine industries [1–4]. Stainless steels [5], aluminum [6,7], titanium [7,8], and nickel alloys [4] are regularly printed to make customized parts and other important components on demand [9], such as patient-specific medical implants [10]. Starting with a three-dimensional digital drawing of the part, metals are deposited layer by layer, often thinner than human hair, to form components [3]. However, after about a quarter of a century of research and development, only a handful of commercial alloys can be additively manufactured, and the market value of all such products now amounts to a negligible portion of the manufacturing economy [4]. This difficulty is largely attributable to the susceptibility to common defects, such as porosity, cracking, lack of fusion, balling, and surface roughness [3,4]. These defects affect part quality, reliability, and serviceability, and often lead to part rejection. In addition, some defects require post-processing of the part which increases cost. Therefore, AM of

defect-free, high-quality parts in a time-efficient and cost-effective way is a major challenge to the materials community [1,2,4].

Currently, defects are minimized by using the traditional approach of optimizing processing conditions by trial and error [11–26]. This technique is not optimum for AM because of the need to conduct many experiments to explore a large range of process parameters and high costs of feedstock and machines combined with a changing economic culture where new products are rapidly created. In addition, trial-and-error tests do not always achieve the desired conditions to mitigate defects because of the complex nature of AM process. Prediction and control of defects require both theories of metallurgy and knowledge of how the process conditions and alloy properties affect the mechanisms of defect formation [3,4]. Mechanistic models of AM processes can predict physical attributes that affect defect formation such as the temperature and velocity fields, molten pool geometry, cooling rates based on process variables, and thermophysical properties of alloys using phenomenological understanding [27–44]. If this understanding is lacking but data are available on process conditions, alloy properties, and defect formation, machine learning [45,46] can make valuable contributions to control the defect formation in AM [47–58]. A synergistic application where the machine learning is trained using the data that capture the physics behind the defect

* Corresponding author.

Table 1
Individual use of experimental trials, mechanistic models, and machine learning to reduce balling as reported in the literature.

Approaches	Examples	Refs.
Experimental trials	Balls can be reduced if scanning speed is less than 1900 mm/s in AlSi10Mg parts.	[11]
	Laser power greater than 75 W and scanning speed less than 290 mm/s can prevent balling in SS316 parts.	[12]
	Balls can be avoided when scanning speed is greater than 60 mm/s in Co-Cr alloys.	[14]
	A decrease in molten pool width and depth can cause balling for IN718 powders.	[16]
	A very low laser power of 159 W and a high speed of 0.6 m/s can result in limited fusion of the substrate which may cause balls in SS316 alloy.	[19]
	A low energy density with laser power of 60 W and scanning speed of 100 mm/s can result in process instability and balls in the L-PBF of SS316 parts.	[20]
	Liquid particles released from the melt pool by the evaporation-driven gas flux, coupled with hydrodynamic instability may cause balls for austenitic stainless steel.	[21]
	Balls can be reduced if the energy input is in the range of 1400–1700 J/mm^3 in EOS PH1 stainless steel for L-PBF.	[22]
	A low energy density may cause balling in steel powder for L-PBF.	[23]
Mechanistic models	A surface model indicates that decreasing heat treatment temperature can reduce balls for Ti-6Al-4 V powder in the L-PBF process.	[27]
	The local part geometry, such as staircase, may cause balling in AlSi10Mg parts estimated by a roughness prediction model.	[28]
	Very low laser power may result in balling because the substrate is not melted explained by a heat source mesoscale model for SS316L parts.	[29]
	Balling can be caused by surface tension's tendency to minimize surfaces and create liquid spheres, Marangoni effect, and vapor recoil pressure with liquid metal ejection in L-PBF of SS316L alloy by a 3D, powder-scale model.	[30]
	A thermal model shows that PBF parts are susceptible to balling when the ratio of pool length to pool width is greater than 2.3.	[31]
	The shrinking tendency of pool induced by surface tension, and a large molten pool to depth ratio (greater than π) may result in balls for Ti6Al4V alloy using five heat source models.	[32]
	Multi-physics models show that balls can be caused by Plateau-Rayleigh instability for SS316 parts for selective laser melting (SLM).	[33]
	A thermal model shows the volumetric energy density and the Plateau-Rayleigh capillary instability are the essential causes of balling formation for SS316 alloy.	[34]
	Balling may be caused by the Kelvin-Helmholtz instability estimated by a comprehensive computational model for GTA welding.	[35]
Machine learning	Convolution neural networks can detect balling with temporal vision information, but cannot predict and reduce balling which is more difficult for SS316L powders.	[20]
	Logistic regression is used to classify balling from other defects in steel components during L-PBF, which can not predict balling before experiments.	[23]
	An artificial neural network is applied to predict surface roughness with considering the heat treatment, laser power, scan pattern angle, and scan speed of Ti-6Al-4V alloy for L-PBF, but cannot reveal the mechanisms of balling.	[27]
	A deep learning convolution neural network can detect and monitor the balling formation for Ti-6Al-4V and nickel alloys, but cannot predict and reduce balling.	[47]
	Surface roughness is estimated for different machining processes by regression analysis, but no available ways to predict and reduce balling.	[48]
	Surface texture and balling were predicted using surface images by Gaussian process regression model for Ti-6Al-4V parts, no practical ways to reduce balls.	[49]
	Balling instability is examined and identified by observing melt pool features in the Inconel 718 parts for the L-PBF process, but the balling prediction is not available.	[50]

formation (physics-informed machine learning) and are computed using a mechanistic model [43,44], can provide important quantitative correlations between the process attributes and defect formation. Such correlations are important because they can reduce the number of experiments needed to achieve low defect, high-quality AM parts. Here we explain the applicability, benefits, and fidelity of the approach of combining physics-informed machine learning, mechanistic modeling, and experimental data to reduce defects in AM by considering an example of a balling defect in laser-assisted powder bed fusion (L-PBF) for which experimental data are available in the literature [11–16].

Balling defects can occur under some undesirable process conditions when the molten pool may suffer from instability and disintegrate into several small, disconnected beads or balls appearing on the component surfaces [3,4]. The formation of balls can require post-processing, reduce dimensional accuracy, degrade fatigue properties, and may hinder the movement of powder spreading roller which interrupts the process [3,4]. Several examples of experimental trials [11–26], the use of mechanistic models [27–44], and machine learning [47–58] to adjust process parameters for reducing balling defects are provided in Table 1. Efforts have been made to explore the mechanistic factors impacting balling defects. Heat energy per unit volume of material deposited controls the melting of alloy powders which affects the balling defect [17,33,49,50,59]. Similarly, surface tension force on the top surface of the molten pool and convective flow of molten metal have been related to the mechanism of ball formation [15,16,19,25,27–30,33,60–62]. Furthermore, balls are formed by the disintegration

of the molten pool due to the hydrodynamic [21,35] and capillary instabilities [30–34,43,50]. These important factors are quantified in the literature and their values have been evaluated for various experimental conditions and alloy compositions using mechanistic models (Table 1) to reduce balling defect. All of these factors depend on the alloy compositions and process parameters, and the effects of each factor on balling defects have been studied separately. However, the combined effects of these important factors on balling defects during L-PBF have not been investigated.

Here we show that the approach of combining physics-informed machine learning, mechanistic modeling, and experimental data can reduce defects in AM by considering an example of a common balling defect in L-PBF. The physics of balling captured through the computed values of the mechanistic variables is analyzed by a physics-informed machine learning to correlate with the balling occurrence data of one hundred and sixty-six independent experiments for six commonly used alloys: AlSi10Mg [11], aluminum 357 [11], stainless steel 316 [12,13], Co-Cr [14], Ti6Al4V [15] and Inconel 718 [16]. Based on this approach (Fig. 1) of combining experimental data, mechanistic modeling, and physics-informed machine learning, we develop an easy-to-use, verifiable balling susceptibility index that can be used to predict and prevent balling in L-PBF. In addition, we investigate the hierarchical importance of the mechanistic variables on balling and present balling susceptibility maps for six alloys. The approach used here can help to reduce other common defects in AM such as cracking, porosity, lack of fusion, and surface roughness for producing defect-free L-PBF components.
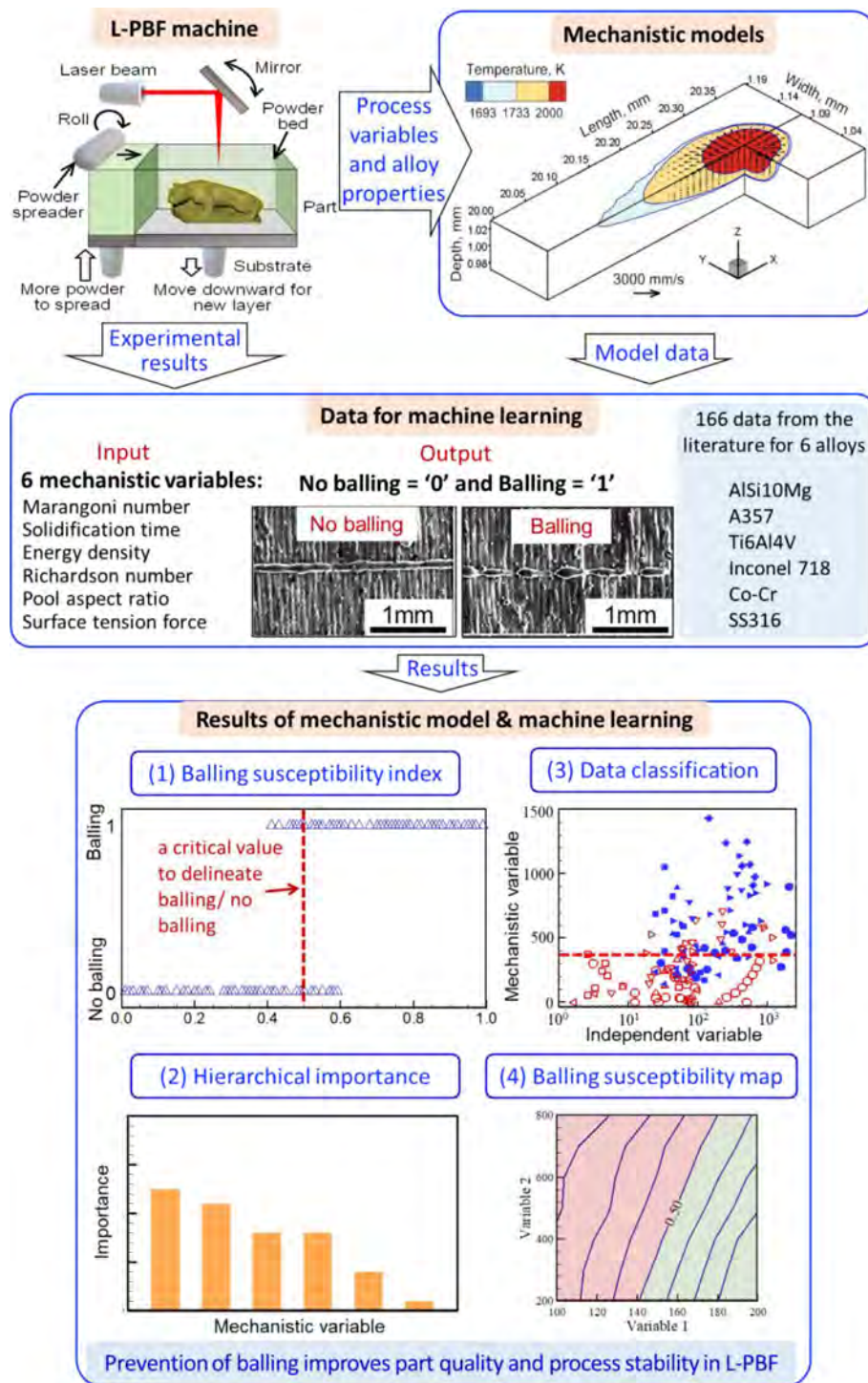
Fig. 1. A schematic representation of the approach proposed and used in this research. The use of experimental results, mechanistic models, and physics-informed machine learning. The use of volumetric energy density, surface tension force, Marangoni number, Richardson number, pool aspect ratio (pool length/pool depth), and the solidification time computed using a mechanistic model of L-PBF in machine learning can predict balling defect. The approach of combining experimental results, mechanistic models and machine learning provides an easy-to-use balling susceptibility index to identify conditions for avoiding balling, hierarchical importance of variables on the balling defect, and balling susceptibility maps. The experimental results of 'No balling' and 'Balling' cases are adapted from [16].

2. Materials and methods

2.1. Why is physics-informed machine learning needed?

Since the effects of process parameters and alloy properties are important for controlling the quality of the AM parts, it is intu-itive to try to correlate them with the occurrence of balling de-fects. The process parameters are easy to measure during the ex-periments, and material properties for common alloys are readily available in the literature. The ten most important parameters in-clude laser power, scan speed, powder diameter, beam diameter, layer thickness, thermal diffusivity of alloy and shielding gas, sur-

Table 2

Ranges of process parameters, material properties, and six mechanistic variables [11–16].

Processed variables and alloy properties		Mechanistic variables	
Parameters (unit)	Range	Variables (unit)	Range
Powder size (μm)	30–75	Vol. Energy density, E (J/mm^3)	1.68–672.45
Laser power (W)	25–500	Surface tension force, F (N)	4.77×10^{-5} – 4.57×10^{-3}
Scan speed (mm/s)	20–3000	Marangoni number, M	1–2090
Beam diameter (mm)	0.08–0.8	Richardson number, R	6.81×10^{-6} – 5.83
Layer thickness (mm)	0.03–0.25	Aspect ratio of pool, ε	1–12.76
Thermal diffusivity of alloy at room temperature (m^2/s)	2.90×10^{-6} – 7.74×10^{-5}	Solidification time of molten pool, T (s)	8.33×10^{-5} – 0.27
Surface tension force of alloy (N/m)	0.82–1.85		
Latent heat of fusion of alloy (J/kg)	2.09×10^5 – 5×10^5		
Liquidus temperature of alloy (K)	867–1928		
Thermal diffusivity of gas (m^2/s)	1.99×10^{-5} – 3.49×10^{-5}		

Table 3

Thermophysical properties of six alloys used in this work. 'T' represents the temperature in K which varies between room temperature and solidus temperature [3,4]. Density and diffusivity values are given at room temperature. Viscosity, surface tension, and dγ/dT, where γ is surface tension and T is temperature are given at the liquidus temperature of alloys.

Properties	SS316	Ti-6Al-4V	IN718	Co-Cr	A357	AlSi10Mg
Liquidus temperature (K)	1733	1928	1609	1703	883	867
Solidus temperature (K)	1693	1878	1533	1603	855	831
Thermal conductivity (W/m K)	11.82 + 0.0106T	$1.57 + 1.6 \times 10^{-2}T-1 \times 10^{-6}$T^2	$0.56+2.9 \times 10^{-2}$T-7×10^{-6}T^2	$-0.923+4.15 \times 10^{-2}T-1 \times 10^{-5}$T^2	$25.2+0.4$T$+7.4 \times 10^{-6}$T^2	$113+1.06 \times 10^{-5}$T
Specific heat (J/ kg K)	$330.9+0.563$T-4.015×10^{-4}T$^2+9.465 \times 10^{-8}$T^3	$492.4+0.025$T-4.18×10^{-6}T^2	$360.4+0.026$T-4×10^{-6}T^2	$387.4+0.2$T-9×10^{-6}T^2	$928.6-0.6$T $+1.5 \times 10^{-3}$T^2	$536.2+ 0.035$T
Density (kg/m^3)	7800	4430	8100	8280	2700	2670
Viscosity (kg/m s)	7×10^{-3}	4×10^{-3}	5×10^{-3}	5×10^{-3}	1.3×10^{-3}	1.3×10^{-3}
Surface tension (N/m)	1.50	1.52	1.82	1.85	0.92	0.82
Thermal diffusivity of alloy (m^2/s)	4.12×10^{-6}	3.14×10^{-6}	2.90×10^{-6}	3.77×10^{-6}	6.84×10^{-5}	7.74×10^{-5}
Latent heat of fusion of alloy (J/kg)	2.72×10^5	2.84×10^5	2.09×10^5	3.14×10^5	5×10^5	4.23×10^5
dγ/dT (N/m K)	-0.40×10^{-3}	-0.26×10^{-3}	-0.37×10^{-3}	-0.37×10^{-3}	-0.35×10^{-3}	-0.35×10^{-3}

face tension force of alloy, latent heat of alloy, liquidus temperature of alloy [3,4]. Process parameters corresponding to one hundred and sixty-six experimental data sets are provided in the Supplementary document. The range of process parameters and material properties are listed in Table 2. Thermo-physical properties of six alloys investigated in this work are available in Table 3. To resolve the roles of these parameters on the balling defect, we need a minimum of 2^{10} (1024) reproducible experiments based on the L2 design of experiments [63]. In addition, no comprehensive investigation of the roles of process parameters and alloy properties would provide any insight into the mechanism of balling. Therefore, the process parameters and alloy properties are not suitable to use in machine learning to forecast balling using the available pool of literature data.

A solution is to use mechanistic variables that represent the physics of the problem. A similar example can be found in the flow of a Newtonian fluid through a pipe. The structure of the flow, laminar or turbulent, is best determined by Reynolds number rather than the individual values of velocity, density, and viscosity of the fluid and the pipe diameter [51]. In AM, several mechanistic variables have been related to the balling defect. They include volumetric energy density, surface tension force, Marangoni number, Kelvin Helmholtz hydrodynamic instability represented by Richardson number, capillary instability represented by pool aspect ratio (pool length/pool depth), and solidification time of the pool. These six mechanistic variables need only 2^6 (64) experimental data points to forecast their effects on balling defects. These mechanistic variables can be calculated using a heat transfer and fluid flow model which involves process parameters and alloy properties. It will be shown that a physics-informed machine learning that relies on the computed values of mechanistic variables can

forecast balling (Fig. 1) and provide mechanistic insights that cannot be obtained by any other means.

Physics informed machine learning correlates the balling defect with mechanistic variables that can reveal the mechanisms of balling based on the laws of physics. For example, the pool aspect ratio (pool length/pool depth), and other variables computed using principles of physics can then be analyzed using machine learning to correlate them with the occurrence of balling. A high pool aspect ratio indicates high Plateau Raleigh capillary instability which makes the pool likely to separate into small spherical balls to maintain the uniform capillary pressure inside the pool. All six mechanistic variables can be calculated using a well-tested mechanistic model that includes all process parameters, alloy properties, and gas properties as required inputs.

The use of physics informed machine learning based on the computed mechanistic variables reduces the amount of required experimental data, lowers the cost, takes the benefit of awesome software and hardware capability of the digital age, makes use of the rich knowledge base of metallurgy, and provides important insight about the mechanisms of balling that cannot be uncovered otherwise.

2.2. Data sets for machine learning

The method relies on 166 data sets from peer-reviewed articles [11–16]. Each experimental test contains a group of high-quality data of cases with the presence and absence of balling defects. Among 166 data sets, 81 cases with balling, and 85 cases where balling were not detected experimentally [11–16]. The case number of each alloy is summarized in the Supplementary document. Six mechanistic variables are found to be related to the mechanism of
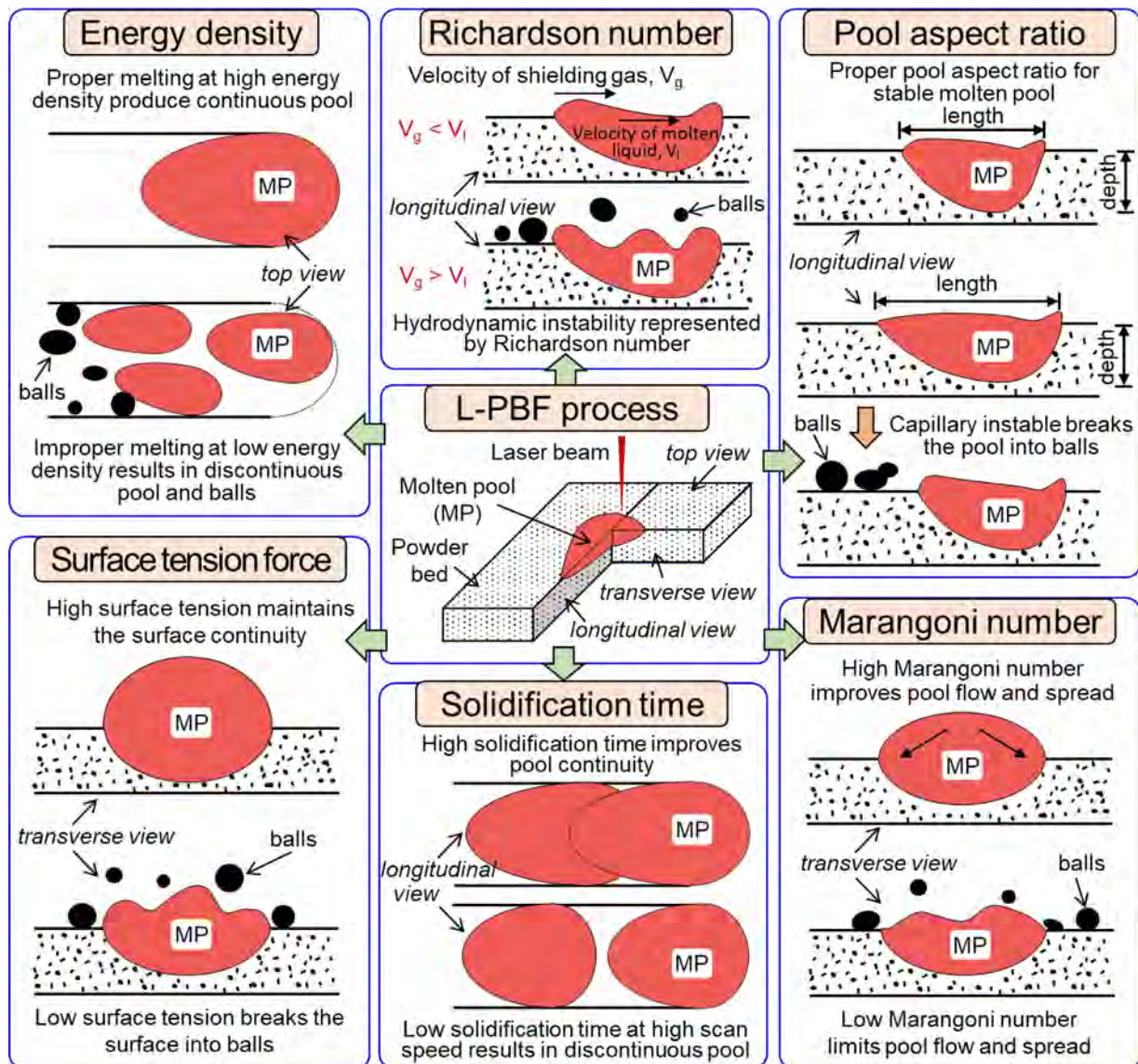
Fig. 2. Effect of the six mechanistic variables on balling defect in L-PBF. The schematic in the center shows the L-PBF process where a laser beam melts alloy powders and produces a molten pool consisting of fusion zone, molten pool (red region). The effects of energy density (E), surface tension force (F), Richardson number (R), solidification time (T), pool aspect ratio (ε), and Marangoni number (M) are shown from left to right. The top left figure showing balls formation due to insufficient energy density [11–19,22–25,28,30,33,49,50,59]. The bottom left figure indicates the low surface tension can cause balling [15,16,19,25,27–30,33,60–62]. Balls can be formed by high hydrodynamic [21,35] and capillary instabilities [13,30–34,61,62] in the top of the middle and right columns. Fast solidification with limited time for pool existing and spreading can result in discontinuous pool and balls [18,20,24,25,43,49] in the bottom of the middle column. Liquid metal flows with low velocity and low Marangoni number are prone to balls in bottom of right column [11,18,27,29,43,62] (For interpretation of the references to color in this figure legend, the reader is referred to the web version of this article.).

balling defect formation (Section 2.3). Each of the data set consists of six computed mechanistic variables along with the absence or presence of balling. The 166 experimental data sets are all marked with '0' or '1' to represent the absence or presence of balling, respectively. Ranges of process parameters, alloy properties, and six computed mechanistic variables corresponding to the 166 experimental data sets are provided in Table 2. Thermo-physical properties of six alloys investigated in this work are available in Table 3. Values of process parameters, gas properties, and six mechanistic variables corresponding to 166 data sets are provided in the Supplementary document.

2.3. Six mechanistic variables and their calculation using a heat transfer and fluid flow model

The six mechanistic variables (Fig. 2) that have been related to the mechanisms of balling are volumetric energy den-

sity [11–19,22–25,28,30,33,49,50,59], Richardson number [21,35], pool aspect ratio (pool length/pool depth) [13,15,16,18,19,23,24,30–34,43,50,61,62,64,65], Marangoni number [11,18,27,29,43,62], solidification time of pool [18,20,24,25,43,49] and surface tension force [15,16,19,25,27–30,33,60–62]. The values of the six mechanistic variables are computed using a well-tested, 3D, transient, heat transfer, and fluid flow model of L-PBF [43,44]. The inputs to the model are the process parameters, alloy, and gas properties, while the outputs from the model include the temperature and velocity fields in three dimensions from which the six mechanistic variables are estimated. Details of explanation and validation about the model are described in previous publications [43,44] and are not repeated here. Only the salient features are indicated here. The model is applied in a 3D solution domain containing the substrate, power bed, deposited tracks, and shielding gas. The calculations are performed using an in-house Fortran code compiled using an Intel Fortran compiler. The temperature-dependent thermophysi-

cal properties of the six alloys are provided in Table 3. The model was run for all 166 experimental cases to calculate the mechanistic variables.

The effects of the six mechanistic variables on balling (Fig. 2) and their calculations using the heat transfer and fluid flow model are described below.

The volumetric energy density (E): Low energy density at a low laser power and rapid scanning speed provides too little energy input per unit length. The insufficient energy to form a proper molten pool results in a discontinuous molten pool that solidify with several small balls (Fig. 2, top left) [11–19,22–25,28,30,33,49,50,59]. The volumetric energy density (E) is expressed as [3,4].

$$E = \frac{P}{v(\pi r^2)} \tag{1}$$

where P is laser power, v is scanning speed, and r is laser beam radius. This represents the amount of energy supplied from the laser heat source per unit volume of material deposited.

Richardson number (R): Balls may form because of the segregation of the pool due to its instability. The Kelvin Helmholtz hydrodynamic instability is caused by the difference between the velocities of shielding gas and the convective flow of liquid metal on the top surface of the molten pool (Fig. 2, top middle). The resulting deposit appears similar to what is observed as the humping effect in fusion welding [36,37,40]. However, the literature from which we collected the experimental data, termed this defect as balling. This hydrodynamic instability can be represented by a dimensionless number called the Richardson number [21,35]. The susceptibility to the balling defect increases with Richardson number due to high pool instability [35]. Richardson number (R) can be calculated as [3,35].

$$R = \frac{gL}{(U_g - U_l)^2} \tag{2}$$

where g is the acceleration due to gravity, L is the pool length that can be calculated using the 3D, transient, heat transfer, and fluid flow model. U_g is the velocity of shielding gas, for L-PBF, which is assumed to be equal to the scanning speed. U_l is the maximum velocity of the convective flow of the liquid metal. The maximum velocity is found on the top surface of the pool along the scanning direction.

Pool aspect ratio (ε): Similar to the hydrodynamic instability, capillary instability can also disintegrate a molten pool and cause balling. Capillary instability of the molten pool is quantified by the pool aspect ratio, which is a ratio of pool length to pool depth (Fig. 2, top right). When the length of the molten pool is significantly larger than its depth (high aspect ratio), the pool becomes unstable and breaks into small balls [13,15,16,18,19,23,24,30–34,43,50,61,62,64,65]. Pool aspect ratio (ε) is expressed by the ratio of pool length to the pool depth. Both pool length and pool depth can be calculated using the 3D, transient, heat transfer, and fluid flow model for different process conditions and alloys.

Surface tension force (F): Surface tension maintains the integrity of the top surface of the molten pool (Fig. 2, bottom left). At low surface tension force, the molten pool may be disintegrated and forms balls [15,16,19,25,27–30,33,60–62]. Surface tension force (F) is calculated as the product of the coefficient of surface tension of an alloy and the circumference of the molten pool on the top surface. The coefficient of surface tension of the six alloys is provided in Table 3. The circumference of the molten pool is calculated on the top surface assuming the pool be an ellipse. The major and minor axes of the elliptical pool are assumed to be the pool length and width, respectively, both of which can be calculated using the 3D, transient, heat transfer, and fluid flow model.

Solidification time of molten pool (T): A molten pool that solidifies rapidly may not allow the molten pool to spread uniformly, breaks into small isolated balls, and forms a discontinuous track (Fig. 2, bottom middle). The solidification time of the molten pool can be represented as the ratio of pool length to the scanning speed [18,20,24,25,43,49]. Solidification time (T) is represented by the ratio of pool length to the scanning speed [3,4]. Pool length can be calculated using the 3D, transient, heat transfer, and fluid flow model.

Marangoni number (M): Convective flow of liquid metal driven primarily by the surface tension gradient on the top surface of the molten pool, helps the molten metal spread uniformly to maintain the continuity of the pool. This convective flow is also known as Marangoni flow, represented by the Marangoni number (Fig. 2, bottom right). A low Marangoni number represents a weak convective flow that is insufficient for uniform spreading of molten liquid which may cause balling defect [11,18,27,29,43,62]. Marangoni number (M) can be calculated as [3,4].

$$Ma = -\frac{d\gamma}{dT} \frac{L\Delta T}{\mu\alpha} \tag{3}$$

where, T, μ, and α are surface tension, temperature, viscosity, and thermal diffusivity of the alloy, respectively. The values of these parameters are provided in Table 3 for the six alloys. L is the pool length which can be calculated using the 3D, transient, heat transfer, and fluid flow model. ΔT is the difference between the maximum temperature inside the pool and the solidus temperature of an alloy. The solidus temperature for six alloys is provided in Table 3. The maximum temperature inside the pool can be calculated using the 3D, transient, heat transfer, and fluid flow model.

2.4. Derivation of balling susceptibility index using a genetic algorithm

The balling susceptibility index (BSI) was derived from the 166 sets of computed values of six mechanistic variables and the experimentally observed ball formation using a genetic algorithm [66,67]. The cases with the absence or presence of ball formation are marked as either '0' or '1' depending on the balling susceptibility of the alloy and process conditions. A genetic algorithm is applied to optimize the values of the coefficients of each mechanistic variable. The objective function for the genetic algorithm is a linear equation connecting the six mechanistic variables and balling. The genetic algorithm provides the coefficients corresponding to each variable for BSI for the six mechanistic variables (Table 2). The coefficients of which have the minimum square error in fitting the balling results using the six mechanistic variables are selected. The best set of parameters obtained from the genetic algorithm were the same as those calculated from a linear regression in MS Excel as well as by pseudo-inverse matrix solution using the well-known Moore–Penrose method.

After mathematical derivation, the BSI is validated and tested with the corresponding validation and testing data sets. Both the validation and testing data sets are selected randomly for the cases with the presence and absence of balling. A threshold value is selected which has the minimum classification error with the minimum number of wrongly predicted data points among 166 data points. For both the validation and testing data sets, the calculated BSI values are compared to the threshold value and classified into '1' (if BSI value is greater than the threshold) and '0' (if BSI value is less than the threshold) for cases with and without balling, respectively, then compared the prediction results of BSI with the target balling results from experimental tests for prediction accuracy of BSI.
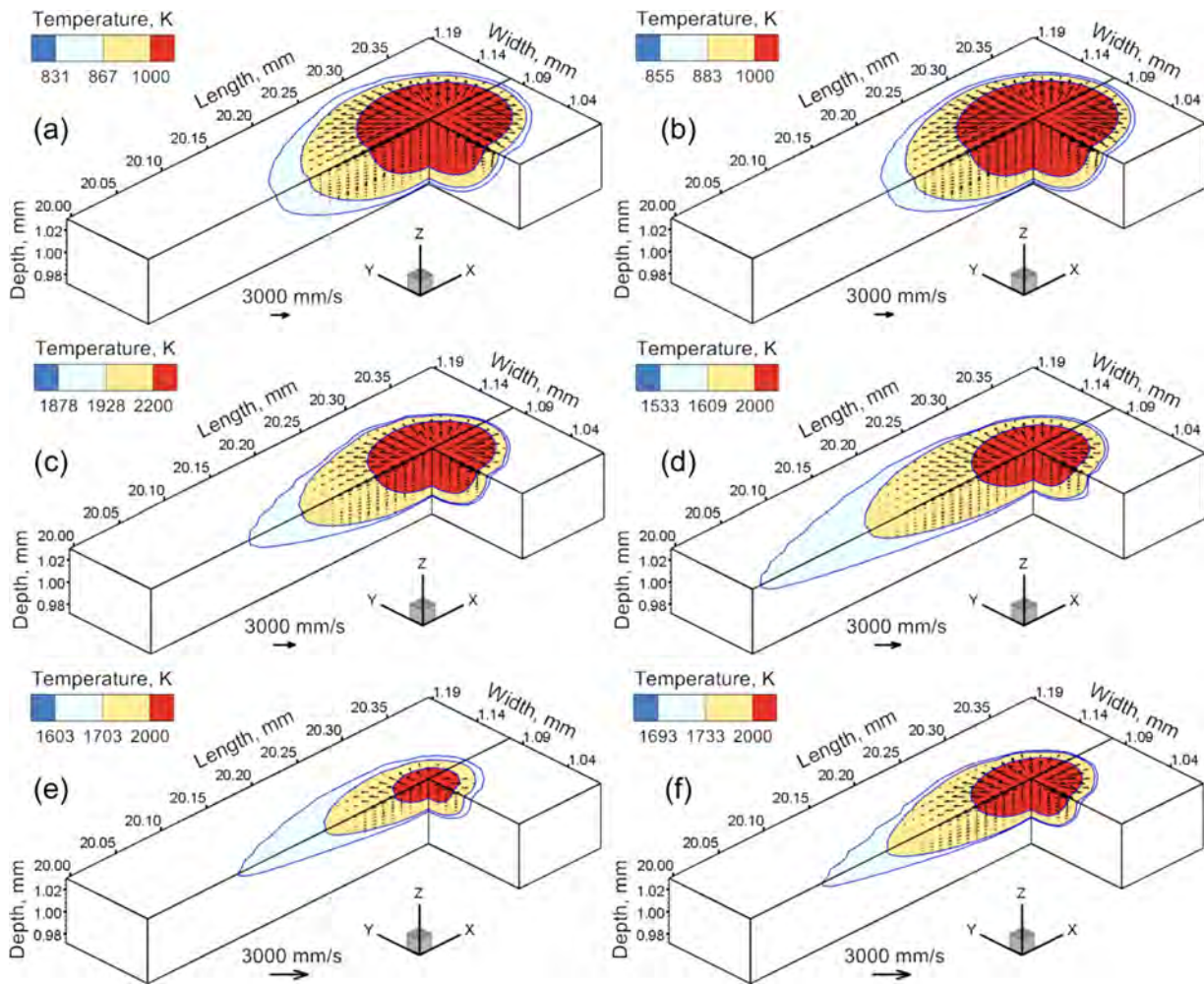
Fig. 3. 3D temperature and velocity distributions calculated using a heat transfer and fluid flow model for six alloys. The results are for 20 mm long single-track builds of (a) AlSi10Mg (b) A357 (c) Ti6Al4V (d) Inconel 718 (e) Co-Cr (f) stainless steel 316 made by L-PBF using 60 W laser power, 1000 mm/s scanning speed, and 30 μm layer thickness and 50 μm beam radius. The scanning direction of the laser beam is along the positive X direction. Y and Z directions represent the width and depth direction, respectively. Temperature values of the contour can be predicted from the temperature contour legend provided in each figure. Black arrows in the figures represent the velocity vectors whose magnitude can be estimated by comparing lengths with the reference vector provided.
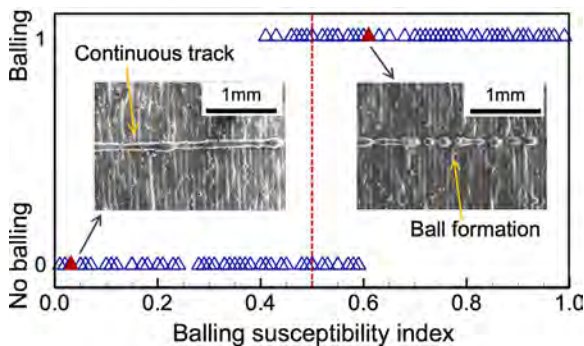
Fig. 4. Balling Susceptibility Index (BSI) to predict balling in L-PBF. The index is calculated using Eq. (4) which is valid for the range of volumetric energy density (E) 1.68 to 672.45 J/mm³, surface tension force (F) 4.77 × 10⁻⁵ to 4.57 × 10⁻³ N, Richardson number (R) 6.81 × 10⁻⁶ to 5.83, solidification time (T) 8.33 × 10⁻⁵ to 0.27 s, aspect ratio of the pool (ε, pool length/depth) 1 to 12.76 and Marangoni number (M) 1 to 2090. The figure shows the index values corresponding to the 166 experimental cases. The threshold value of the balling susceptibility index (0.5) which delineates the balling and no balling cases is indicated by a vertical red dashed line. Two insets with the presence and absence of balls for L-PBF of Inconel 718 alloy are shown corresponding to two data points of balling susceptibility index [16]. The ranges of six mechanistic variables are provided in Table 2 (For interpretation of the references to color in this figure legend, the reader is referred to the web version of this article.).

2.5. Calculations of hierarchical importance using feature selection indexes

The hierarchical importance of the six mechanistic variables on ball formation is evaluated by the relative importance of each variable in BSI, as well as three feature selection indexes, information gain (IG), information gain ratio (IG ratio), and Gini index [52,68]. These three indexes rely on the threshold values of the mechanistic variables that approximately delineate between the cases with balling and the cases where balling is not observed. The hierarchical importance is estimated using the 166 sets of computed values of six mechanistic variables and the experimentally observed balling ('0' or '1'). The high values of information gain and information gain ratio show more importance which are calculated based on entropy [52,68]. In contrast, low values of the Gini index show more importance [52,68]. A set of sample calculations of hierarchical importance using the three algorithms are provided in the Supplementary document.

3. Results and discussion

The six mechanistic variables used here, volumetric energy density, surface tension force, Marangoni number, Richardson number, pool aspect ratio (pool length/pool depth), and solidification
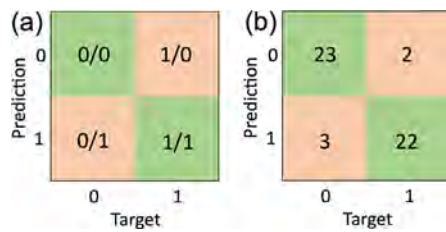
Fig. 5. Balling formation prediction ability of the machine learning. The matrices shown in the figure are called confusion matrices commonly used to visually represent the prediction ability of a machine learning algorithm. (a) The basic structure of a confusion matrix. 'Target' represents the target output of the machine learning which is the experimental observation of balling. '0' and '1' indicate the absence and presence of balling in the part respectively. 'Prediction' represents the predicted output by machine learning. The Top left green box '0/0' represents how many '0' cases are predicted correctly. The bottom right green box '1/1' represents how many '1' cases are predicted correctly. The top right orange box '1/0' represents the number of cases where experimental observation is '1' but machine learning wrongly predicts them '0'. The bottom left orange box '0/1' represents the number of cases where experimental observation is '0' but machine learning wrongly predicts them '1'. Accuracy of prediction can be calculated as (total numbers in top left and bottom right green boxes)/ (total number of cases). Sensitivity is calculated as (the bottom right green boxes)/ (all target balling cases, total of top right and bottom right boxes). Specificity is calculated as (the top left box)/ (all target cases without balling, a total of top left and bottom left boxes). For all 166 data points, 30% are used for testing the dataset (26 cases of '0' and 24 cases of '1'). Confusion matrices are shown for (b) testing results of BSI using six mechanistic variables, with an accuracy of 90%, a sensitivity of 91.6%, and a specificity of 88.4%. The calculations of accuracy, sensitivity, and specificity [51,52,68] are explained in the Supplementary document (For interpretation of the references to color in this figure legend, the reader is referred to the web version of this article.).

time of the pool, can capture the combined effects of process parameters and alloy properties. For example, surface tension force and Marangoni number are found to depend on the laser power, scanning speed, and material properties for AlSi10Mg, A357, and Co-Cr alloys [11,14]. High capillary instability can be caused by rapid scanning for stainless steel 316 [13]. The Kelvin Helmholtz hydrodynamic instability results from improper process conditions [21,35]. The solidification time is found to be related to the scanning speed and material properties [43,44]. The calculated values of six mechanistic variables corresponding to 166 experimental data are available in the Supplementary document, and their ranges are listed in Table 2. The computed molten pool shape and size, and temperature fields (Fig. 3) that affect the six mechanistic variables vary drastically for the six alloys resulting in different susceptibility to balling defect. Any of these six mechanistic variables cannot predict the susceptibility to balling defects individually. However, when they are used together in machine learning, the combined usage of these mechanistic variables can provide a ball susceptibility index to forecast balling before experiments as discussed below.

3.1. Balling susceptibility index and its experimental validation

A balling susceptibility index (BSI) is an easy-to-use indicator that can predict balling defects from the computed values of six mechanistic variables. The BSI is derived by connecting the actual occurrence of balling with the six mechanistic variables for 166 experimental data for six alloys (Supplementary document) using a genetic algorithm. The data collection and implementation of the genetic algorithm are presented in Section 2.

$$BSI = 6.5 \times 10^{-1} + 7.2 \times 10^{-1}R + 4.9 \times 10^{-2}\varepsilon$$
$$-9.3 \times 10^{-4}M - 1.9 \times 10^{-3}E - 9.6 \times 10^{1}F - 4.5T \quad (4)$$

where the variables, R, ε, M, E, F, and T indicate the calculated values of Richardson number, pool aspect ratio, Marangoni number, volumetric energy density (in J/mm^3), surface tension force (in N),
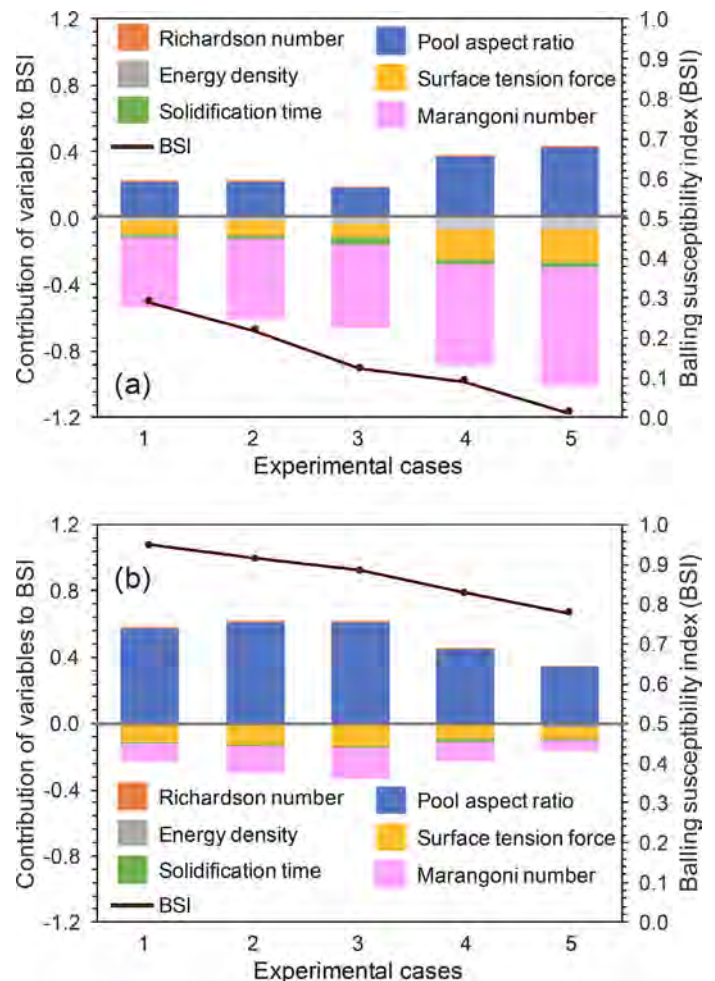
Fig. 6. The relative importance of the six mechanistic variables. The contribution of each of the six mechanistic variables to the balling susceptibility index (BSI) and the values of BSI are shown for five experimental cases [11–16] with both the (a) absence and (b) presence of balling. The beneficial contributions of energy density (grey) and surface tension force (yellow), solidification time (green), and Marangoni number (pink) in preventing balling are due to their negative coefficients in Eq. (4). The balling susceptibility index increases with the increase of Richardson number (orange) and the pool aspect ratio (blue) because of their positive coefficients in Eq. (4). For the absence of balling (Fig. a), the computed BSI values are less than the threshold value of 0.5 (Fig. 4). In contrast, the values of BSI are higher than 0.5 when balling was found (Fig. b) (For interpretation of the references to color in this figure legend, the reader is referred to the web version of this article.).

and solidification time of pool (in s). Eq. (4) is valid for the ranges of the six mechanistic variables (Table 2) and the six alloys investigated [11–16] (Table 3). A high value of BSI indicates high susceptibility to balling defect. The calculated BSI values corresponding to the 166 experimental data points indicate that there is a threshold value of 0.5 which can delineate between the presence and absence of balling with minimum classification error (Fig. 4).

The computed values of BSI can be used to predict balling defects for a new set of process conditions using the six mechanistic variables before doing experiments. With the six mechanistic variables calculated using the well-tested, heat transfer, and fluid flow model of L-PBF, balls may form if the calculated BSI using the computed values of mechanistic variables is higher than 0.5. For example, we consider two sets of experimental data for the presence and absence of the balls in L-PBF of Inconel 718 from the literature [16]. BSI values calculated for these two cases (BSI=0.01 and BSI=0.61) are indicated in Fig. 4 which are consistent with the corresponding experimental evidence. The sign of the coefficients
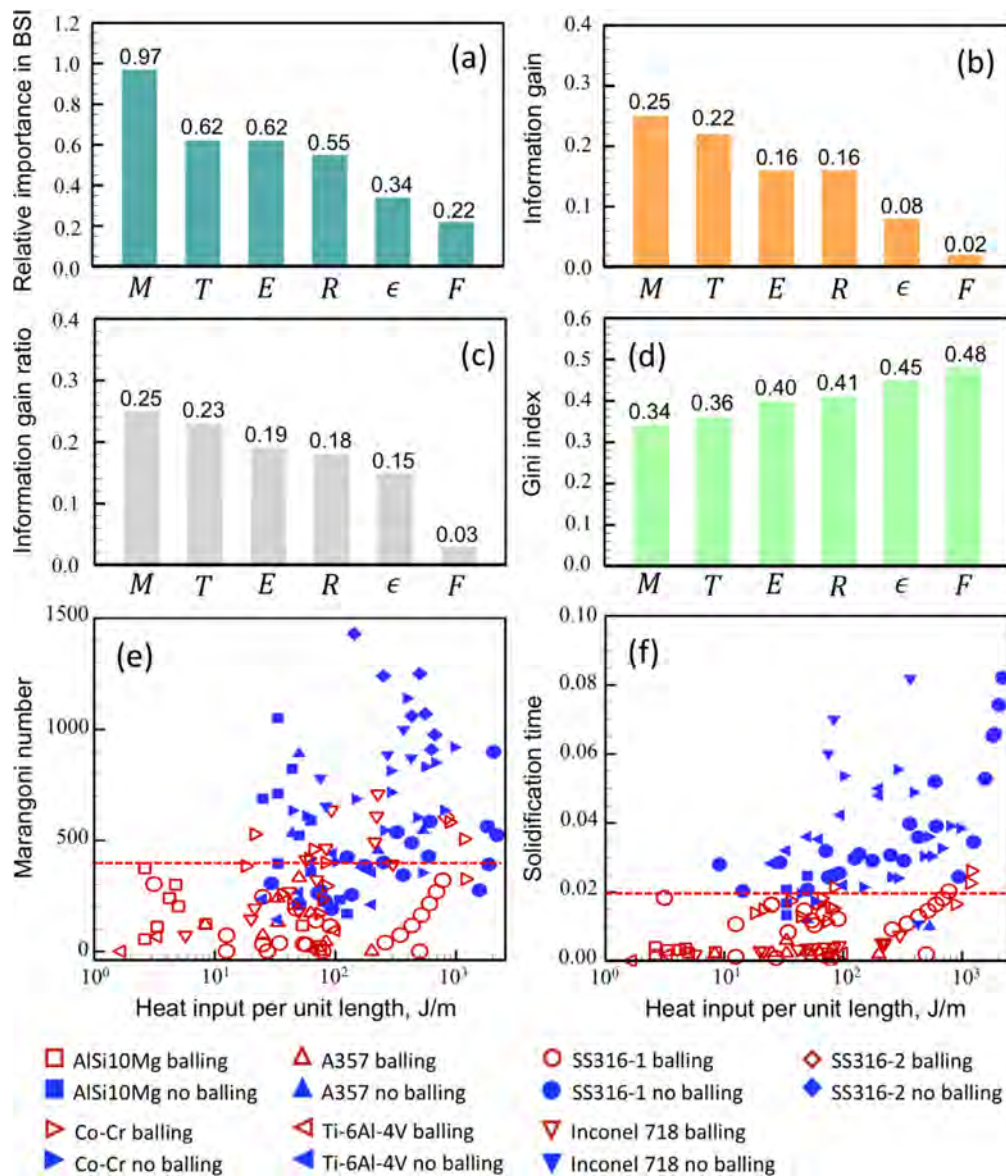
Fig. 7. Hierarchical influence of six mechanistic variables on balling defect and distribution of the two most important mechanistic variables for 166 data. Marangoni number (M), solidification time (T), volumetric energy density (E), Richardson number (R), pool aspect ratio (ε, pool length/depth) and surface tension force (F) have decreasing order of influence on ball formation estimated by (a) the relative importance in BSI equation (coefficient of each variable multiplies the middle-value of the corresponding variable range) and three feature selection indexes (b) information gain, (c) information gain ratio and (d) Gini index. High relative importance in BSI indicates high importance. Both the information gain and information gain ratio are calculated based on entropy, and the higher value indicates higher importance. The Gini index is calculated based on impurity, which has higher importance with a lower value. Distribution of the first and second important mechanistic variables for 166 data are plotted in (e) Marangoni number and (f) solidification time with heat input per unit length (laser power/scanning speed). Horizontal dashed red lines approximately separate values for 'balling' and 'no balling' cases. Two different experimental sets for the same stainless steel 316 alloy are marked as 'SS316-1' and 'SS316-2', respectively. Results for six mechanistic variables are provided in the Supplementary document.

in Eq. (4) indicates how a mechanistic variable influences balling. For example, Richardson number (R) and pool aspect ratio (ε) have positive coefficients which show that balling defect increases at a high value of these two variables. Similarly, negative coefficients of volumetric energy density (E), Marangoni number (M), surface tension force (F), as well as solidification time (T) indicate less chance of balling for their high values. For all 166 data points, 60% of them are used for training dataset (51 cases of '0' and 49 cases of '1'), 10% are used for validation (8 cases of '0' and 8 cases of '1'), and 30% are used for testing dataset (26 cases of '0' and 24 cases of '1'). With rigorous mathematical derivation, validation, and testing, the BSI can forecast balling with 90% accuracy, 91.6% sensitivity, and 88.4% specificity [51,52,68]. The testing result is represented by the confusion matrix in Fig. 5. Details for derivation, validation,

and testing are presented in Section 2. In addition, the relative importance of these six mechanistic variables on balling defects can be estimated as discussed below.

3.2. Hierarchical importance of six mechanistic variables

The relative importance of the six mechanistic variables on balling defects is evident from their relative contributions to BSI (Fig. 6) for several experimental cases with and without ball formation. Here we computed the BSI using Eq. (4) and the contribution of each variable by multiplying their coefficients in Eq. (4) with their computed values corresponding to each experimental case. For the five cases where balls are not detected experimentally, the four variables with negative coefficients have a ben-
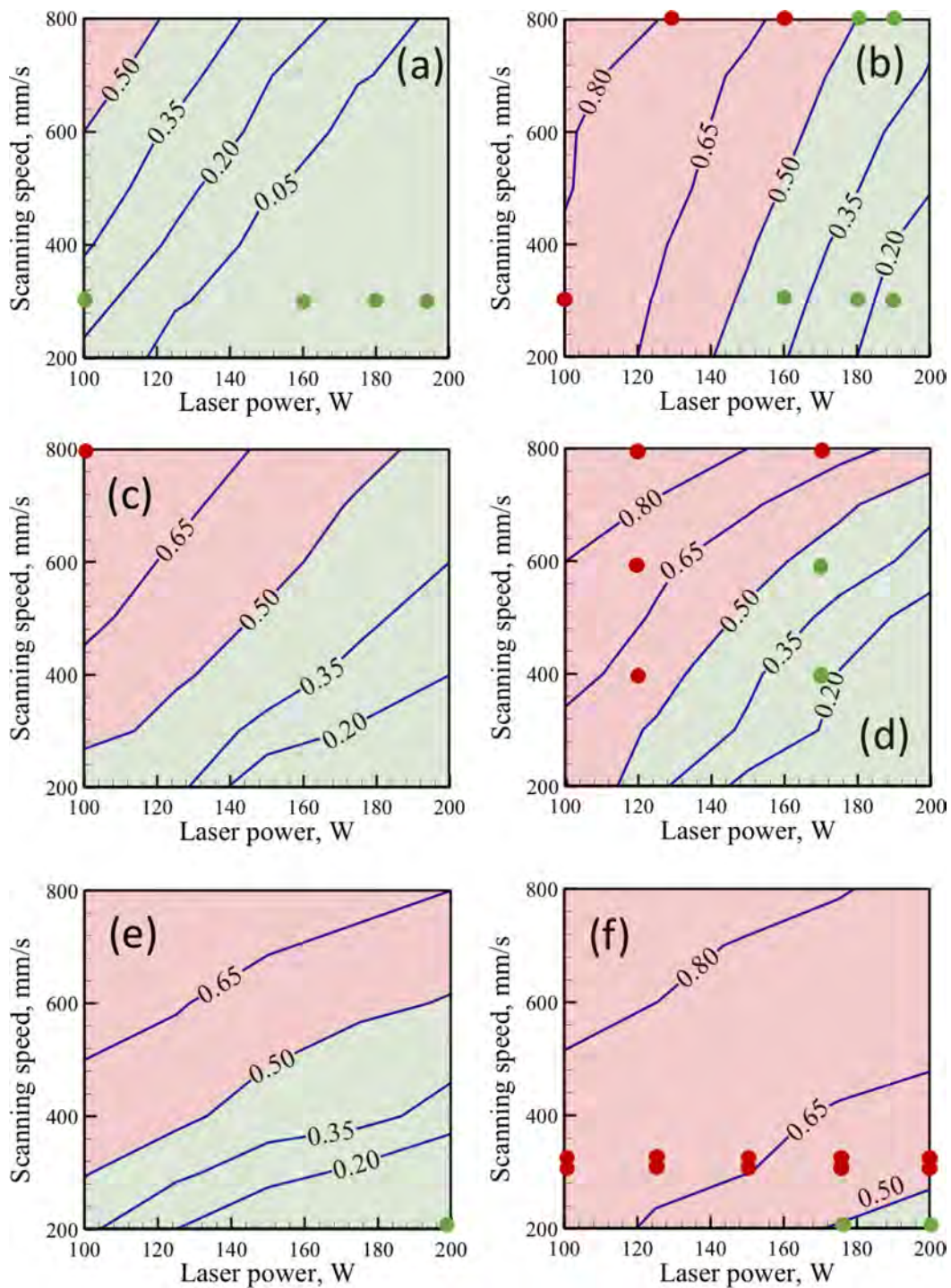
Fig. 8. Balling susceptibility maps and BSI values for six alloys with various process conditions. The results are for 20 mm long single-track builds of (a) AlSi10Mg (b) A357 (c) Ti6Al4V (d) Inconel 718 (e) Co-Cr (f) stainless steel 316 alloys made by L-PBF using the corresponding experimental setting from [11–16]. Ranges of process parameters and material properties are available in Tables 2 and 3. The process conditions which are highly likely for a balling defect with a BSI value higher than 0.5 have been marked with the red region for each alloy. The balling susceptibility maps have been verified by some experimental cases [11–16] for the presence and absence of ball formation with 'red' and 'green' points, respectively (For interpretation of the references to color in this figure legend, the reader is referred to the web version of this article.).

eficial contribution to reduce BSI and prevent balling (Fig. 6 (a)). In the contrast, for the five cases with balling, the two variables with positive coefficients are primarily responsible for increasing the value of BSI and causing balling defects (Fig. 6 (b)).

The relative importance of the six mechanistic variables on balling defects can also be predicted from the coefficients of each variable in Eq. (4) using the coefficients multiplied by the mid-value of the range of the corresponding variable (Table 2). The

Marangoni number is found to be the most important factor that affects balling, followed by the solidification time of the pool and volumetric energy density (Fig. 7 (a)). The surface tension force has the least influence on the balling defect. The same hierarchical importance of the six mechanistic variables on balling defect is also found using three different feature selection indexes in machine learning, information gain (Fig. 7 (b)), information gain ratio (Fig. 7 (c)) and Gini index (Fig. 7 (d)) [52,68]. Calculations

of these three indexes are discussed in Section 2. The Marangoni number has the highest value of both information gain and information gain ratio calculated based on entropy, which indicates the Marangoni number as the most important variable for the balling defect. Similarly, the highest influence of the Marangoni number on balling is evident from its lowest value of the Gini index among the six variables indicating its lowest impurity in data classification. The distribution of the two most important mechanistic variables, Marangoni number and solidification time for 166 data are plotted in Fig. 7 (e) and (f), respectively. Both variables (Fig. 7 (e) and (f)) have shown obvious trends in delineating cases presence and absence of balls formation. The hierarchical importance of variables on balling defects will guide engineers to identify the most important factors to tune in to prevent balls in L-PBF.

3.3. Balling susceptibility maps and their experimental validation

The computed values of BSI for different process conditions and alloys can be used to construct balling susceptibility maps indicating the process windows for preventing balling (Fig. 8). The trends of BSI in these maps are consistent with the common industrial practice. For example, reduction of balling (at low BSI) by ensuring proper melting at high laser power and slow scanning is a well-recognized technique used in additive manufacturing. In the maps, the balling susceptible zones (for BSI > 0.5) are marked with red, and the safe zones (for BSI ≤ 0.5) are marked with green. For the same process window, the balling susceptibility zones (red regions) vary widely indicating a significant contribution of alloy properties on the balling defect. In addition, the balling susceptibility maps for six alloys have been validated by some experimental data [11–16] for the cases with and without balling by the 'red' and 'green' dots, respectively. These maps when rigorously tested against independent experimental data can be made available on the shop floor for real-time prediction of ball formation before performing experiments.

4. Conclusion

We combine physics-informed machine learning, mechanistic modeling, and experimental data to reduce defects in AM by considering an example of balling defects in L-PBF using peer-reviewed experimental data available in the literature. Based on this unique approach, we propose a unified, quantitative framework to uncover the mechanism of balling and reduce defects which cannot be done by any other means. Six important mechanistic variables, volumetric energy density, Marangoni number, solidification time of the pool, surface tension force, Richardson number, and molten pool aspect ratio (pool length/depth) are combined with the balling occurrence data using a physics-informed machine learning algorithm. Below are specific findings.

(1) We propose an easy-to-use, verifiable balling susceptibility index that combines the effects of process parameters and alloy properties. The balling susceptibility index can predict balling defects with 90% accuracy using 166 cases.

(2) The six mechanistic variables reveal the mechanisms of balling defects based on scientific principles with machine learning. The three machine learning indices, information gain, information gain ratio, and Gini index show the same order of hierarchy of the mechanistic variables in influencing balling. The Marangoni number and solidification time are found to be the first and second most important variables on balling, respectively for the alloys and L-PBF process variables investigated here.

(3) We provide six balling susceptibility maps for six commonly used alloys where the trends of the balling susceptibility index with the well-known L-PBF variables are consistent with

the common industrial practice for both fusion welding and additive manufacturing.

The approach used here can help to reduce other common defects in AM such as cracking, porosity, lack of fusion, and surface roughness. Reduction of defects based on scientific principles will improve part quality, reduce cost, and allow printing of new components. In addition, new printable alloys [69] can be discovered to fabricate tailor-made components on demand in a cost-effective way. Similarly, the proposed methodology can be useful for solving other complex engineering problems beyond additive manufacturing and alloys investigated here.

Data availability statement

The raw/processed data required to reproduce these findings cannot be shared at this time due to technical or time limitations.

Declaration of Competing Interest

The authors declare that they have no known competing financial interests or personal relationships that could have appeared to influence the work reported in this paper.

Supplementary materials

Supplementary material associated with this article can be found, in the online version, at doi:10.1016/j.apmt.2021.101123.

CRediT authorship contribution statement

Y. Du: Methodology, Data curation, Formal analysis, Writing – original draft, Software, Validation. **T. Mukherjee:** Conceptualization, Software, Investigation, Writing – original draft. **T. DebRoy:** Conceptualization, Supervision, Writing – review & editing.

References

[1] T. DebRoy, T. Mukherjee, H.L. Wei, J.W. Elmer, J.O. Milewski, Metallurgy, mechanistic models and machine learning in metal printing, Nat. Rev. Mater. 6 (1) (2021) 48–68.

[2] T. DebRoy, T. Mukherjee, J.O. Milewski, et al., Scientific, technological and economic issues in metal printing and their solutions, Nat. Mater. 18 (2019) 1026–1032.

[3] T. DebRoy, H.L. Wei, J.S. Zuback, et al., Additive manufacturing of metallic components – process, structure and properties, Prog. Mater. Sci. 92 (2018) 112–224.

[4] H.L. Wei, T. Mukherjee, W. Zhang, J.S. Zuback, et al., Mechanistic models for additive manufacturing of metallic components, Prog. Mater. Sci. 116 (2021) 100703.

[5] L. Liu, Q. Ding, Y. Zhong, et al., Dislocation network in additive manufactured steel breaks strength–ductility trade-off, Mater. Today 21 (4) (2018) 354–361.

[6] J.H. Martin, B.D. Yahata, J.M. Hundley, et al., 3D printing of high-strength aluminum alloys, Nature 549 (2017) 365–369.

[7] B. Nan, F.J. Galindo-Rosales, J.M. Ferreira, 3D printing vertically: direct ink writing free-standing pillar arrays, Mater. Today. 35 (2020) 16–24.

[8] S. Hocine, H. Van Swygenhoven, S. Van Petegem, et al., Operando X-ray diffraction during laser 3D printing, in: Mater. Today, 34, 2020, pp. 30–40.

[9] S. Zhao, G. Siqueira, S. Drdova, et al., Additive manufacturing of silica aerogels, Nature 584 (2020) 387–392.

[10] S. Bose, S. Vahabzadeh, A. Bandyopadhyay, Bone tissue engineering using 3D printing, Mater. Today 16 (2013) 496–504.

[11] A. Aversa, M. Moshiri, E. Librera, et al., Single scan track analyses on aluminum based powders, J. Mater. Process. Technol. 255 (2018) 17–25.

[12] A. Laohaprapanon, P. Jeamwatthanachai, M. Wongcumchang, et al., Optimal scanning condition of selective laser melting processing with stainless steel 316L powder, Adv. Mater. Res. 341-342 (2012) 816–820.

[13] D. Gu, Y. Shen, Balling phenomena in direct laser sintering of stainless steel powder: metallurgical mechanisms and control methods, Mater. Des. 30 (2009) 2903–2910.

[14] M.H. Hong, B.K. Min, T.Y. Kwon, The influence of process parameters on the surface roughness of a 3D-printed Co–Cr dental alloy produced via selective laser melting, Appl. Sci. 6 (2012) 401.

[15] J.J.S. Dilip, S. Zhang, C. Teng, et al., Influence of processing parameters on the evolution of melt pool, porosity, and microstructures in Ti-6Al-4V alloy parts fabricated by selective laser melting, Prog. Addit. Manuf. 2 (2017) 157–167.

[16] M. Balbaa, S. Mekhiel, M. Elbestawi, et al., On selective laser melting of Inconel 718: densification, surface roughness, and residual stresses, Mater. Des. 193 (2020) 108818.

[17] R. Li, J. Liu, Y. Shi, et al., Balling behavior of stainless steel and nickel powder during selective laser melting process, Int. J. Adv. Manuf. Technol. 59 (2012) 1025–1035.

[18] T. Yang, T. Liu, W. Liao, The influence of process parameters on vertical surface roughness of the AlSi10Mg parts fabricated by selective laser melting, J. Mater. Process. Technol. 266 (2019) 26–36.

[19] V. Gunenthiram, P. Peyre, M. Schneider, et al., Analysis of laser–melt pool–powder bed interaction during the selective laser melting of a stainless steel, J. Laser Appl. 29 (2017) 022303.

[20] Y. Zhang, H.G. Soon, D. Ye, et al., Powder-bed fusion process monitoring by machine vision with hybrid convolutional neural networks, IEEE Trans. Industr. Inform. 16 (2019) 5769–5779.

[21] A. Gusarov, D. Kotoban, I. Zhirnov, Optical diagnostics of selective laser melting and monitoring of single-track formation, Matec. Web Conf. 129 (2017) 01037.

[22] M. Islam, T. Purtonen, H. Piili, et al., Temperature profile and imaging analysis of laser additive manufacturing of stainless steel, Phys. Proced. 41 (2013) 828–835.

[23] G. Repossini, V. Laguzza, M. Grasso, et al., On the use of spatter signature for *in-situ* monitoring of laser powder bed fusion, Addit. Manuf. 16 (2017) 35–48.

[24] S. Liu, H. Guo, Balling behavior of selective laser melting (SLM) magnesium alloy, Materials 13 (2020) 3632.

[25] Y.D. Qiu, J.M. Wu, A.N. Chen, et al., Balling phenomenon and cracks in alumina ceramics prepared by direct selective laser melting assisted with pressure treatment, Ceram. Int. 46 (2020) 13854–13861.

[26] S.A. Tofail, E.P. Koumoulos, A. Bandyopadhyay, et al., Additive manufacturing: scientific and technological challenges, market uptake and opportunities, Mater. Today. 21 (2018) 22–37.

[27] A.M. Khorasani, I. Gibson, A.H. Ghasemi, et al., Modelling of laser powder bed fusion process and analysing the effective parameters on surface characteristics of Ti-6Al-4V, Int. J. Mech. Sci. 168 (2020) 105299.

[28] A. Boschetto, L. Bottini, F. Veniali, Roughness modeling of AlSi10Mg parts fabricated by selective laser melting, J. Mater. Process. Technol. 241 (2017) 154–163.

[29] B. Liu, G. Fang, L. Lei, et al., A new ray tracing heat source model for mesoscale CFD simulation of selective laser melting (SLM), Appl. Math. Model. 79 (2020) 506–520.

[30] S.A. Khairallah, A.T. Anderson, A. Rubenchik, et al., Laser powder-bed fusion additive manufacturing: physics of complex melt flow and formation mechanisms of pores, spatter, and denudation zones, Acta Mater. 108 (2016) 36–45.

[31] L. Johnson, M. Mahmoudi, B. Zhang, et al., Assessing printability maps in additive manufacturing of metal alloys, Acta Mater. 176 (2019) 199–210.

[32] E. Mirkoohi, D.E. Seivers, H. Garmestani, et al., Heat source modeling in selective laser melting, Materials 12 (2019) 2052.

[33] H. Gu, C. Wei, L. Li, et al., Multi-physics modelling of molten pool development and track formation in multi-track, multi-layer and multi-material selective laser melting, Int. J. Heat Mass Transf. 151 (2020) 119458.

[34] E.L. Papazoglou, N.E. Karkalos, A.P. Markopoulos, A comprehensive study on thermal modeling of SLM process under conduction mode using FEM, Int. J. Adv. Manuf. Technol. (2020) 1–17.

[35] A. Kumar, T. DebRoy, Toward a unified model to prevent humping defects in gas tungsten arc welding, Weld. J. 85 (2006) 292–304.

[36] P.F. Mendez, T.W. Eagar, Penetration and defect formation in high-current arc welding, Weld. J. 82 (2003) 296–306.

[37] P.F. Mendez, K.L. Niece, T.W. Eagar, Humping formation in high current GTA welding, in: Proceedings of the International Conference on Joining of Advanced and Specialty Materials II, Cincinnati, 1999.

[38] T.C. Nguyen, D.C. Weckman, D.A. Johnson, et al., The humping phenomenon during high speed gas metal arc welding, Sci. Technol. Weld. Join. 10 (2005) 447–459.

[39] U. Gratzke, P.D. Kapadia, J. Dowden, et al., Theoretical approach to the humping phenomenon in welding processes, J. Phys. D Appl. Phys. 25 (1992) 1640–1647.

[40] E. Soderstrom, P. Mendez, Humping mechanisms present in high speed welding, Sci. Technol. Weld. Join. 11 (2006) 572–579.

[41] X. Meng, G. Qin, Z. Zou, Investigation of humping defect in high speed gas tungsten arc welding by numerical modelling, Mater. Des. 94 (2016) 69–78.

[42] C. Teng, H. Gong, A. Szabo, et al., Simulating melt pool shape and lack of fusion porosity for selective laser melting of cobalt chromium components, J. Manuf. Sci. Eng. 139 (2017) 011009.

[43] T. Mukherjee, H.L. Wei, A. De, et al., Heat and fluid flow in additive manufacturing-Part I: modeling of powder bed fusion, Comput. Mater. Sci. 150 (2018) 304–313.

[44] T. Mukherjee, H.L. Wei, A. De, et al., Heat and fluid flow in additive manufacturing-Part II: powder bed fusion of stainless steel, and titanium, nickel and aluminum base alloys, Comput. Mater. Sci. 150 (2018) 369–380.

[45] G.D. Goh, S.L. Sing, W.Y. Yeong, A review on machine learning in 3D printing: applications, potential, and challenges, Artif. Intell. Rev. 54 (2021) 63–94.

[46] C. Yu, J. Jiang, A perspective on using machine learning in 3D bioprinting, Int. J. Bioprinting 6 (1) (2020) 253.

[47] J. Williams, P. Dryburgh, A. Clare, et al., Defect detection and monitoring in metal additive manufactured parts through deep learning of spatially resolved acoustic spectroscopy signals, Smart Sustain. Manuf. Syst. 2 (2018) 204–226.

[48] R. Kumar, P. Kulashekar, B. Dhanasekar, et al., Application of digital image magnification for surface roughness evaluation using machine vision, Int. J. Mach. Tools Manuf. 45 (2005) 228–234.

[49] V. Akhil, G. Raghav, N. Arunachalam, et al., Image data-based surface texture characterization and prediction using machine learning approaches for additive manufacturing, J. Comput. Inf. Sci. Eng. 20 (2020) 021010.

[50] L. Scime, J. Beuth, Using machine learning to identify *in-situ* melt pool signatures indicative of flaw formation in a laser powder bed fusion additive manufacturing process, Addit. Manuf. 25 (2019) 151–165.

[51] Y. Du, T. Mukherjee, T. DebRoy, Conditions for void formation in friction stir welding from machine learning, NPJ Comput. Mater. 5 (2019) 68.

[52] Y. Du, T. Mukherjee, P. Mitra, et al., Machine learning based hierarchy of causative variables for tool failure in friction stir welding, Acta Mater. 192 (2020) 67–77.

[53] L. Chen, X. Yao, P. Xu, et al., Rapid surface defect identification for additive manufacturing with *in-situ* point cloud processing and machine learning, Virtual Phys. Prototyp 16 (2021) 50–67.

[54] A. Caggiano, J. Zhang, V. Alfieri, et al., Machine learning-based image processing for on-line defect recognition in additive manufacturing, Addit. Manuf. 68 (2019) 451–454.

[55] C. Gobert, E.W. Reutzel, J. Petrich, et al., Application of supervised machine learning for defect detection during metallic powder bed fusion additive manufacturing using high resolution imaging, Addit. Manuf. 21 (2018) 517–528.

[56] C. Xia, Z. Pan, J. Polden, et al., Modelling and prediction of surface roughness in wire arc additive manufacturing using machine learning, J. Intell. Manuf. (2021) 1–16 J. Intell. Manuf..

[57] Q. Zhu, Z. Liu, J. Yan, Machine learning for metal additive manufacturing: predicting temperature and melt pool fluid dynamics using physics-informed neural networks, Comput. Mech. 67 (2) (2021) 619–635.

[58] Z. Zhan, H. Li, Machine learning based fatigue life prediction with effects of additive manufacturing process parameters for printed SS 316L, Int. J. Fatigue 142 (2021) 105941.

[59] P. Karimi, E. Sadeghi, J. Ålgårdh, et al., EBM-manufactured single tracks of Alloy 718: influence of energy input and focus offset on geometrical and microstructural characteristics, Mater. Charact. 148 (2019) 88–99.

[60] M. Skalon, B. Meier, A. Gruberbauer, et al., Stability of a melt pool during 3D-printing of an unsupported steel component and its influence on roughness, Materials 13 (2020) 808.

[61] P. Promoppatum, S.C. Yao, Analytical evaluation of defect generation for selective laser melting of metals, Int. J. Adv. Manuf. Technol. 103 (2019) 1185–1198.

[62] X. Zhou, X. Liu, D. Zhang, et al., Balling phenomena in selective laser melted tungsten, J. Mater. Process. Technol. 222 (2015) 33–42.

[63] J. Antony, Design of Experiments for Engineers and Scientists, Elsevier, Netherlands, 2014.

[64] H.E. Sabzi, P.E.J. Rivera-Díaz-del-Castillo, Defect prevention in selective laser melting components: compositional and process effects, Materials 12 (2019) 3791.

[65] P.J. DePond, G. Guss, S. Ly, et al., *In situ* measurements of layer roughness during laser powder bed fusion additive manufacturing using low coherence scanning interferometry, Mater. Des. 154 (2018) 347–359.

[66] M.T. Bhoskar, M.O.K. Kulkarni, M.N.K. Kulkarni, et al., Genetic algorithm and its applications to mechanical engineering: a review, Mater. Today Proc. 2 (2015) 2624–2630.

[67] C. Hu, Y. Zuo, C. Chen, et al., Genetic algorithm-guided deep learning of grain boundary diagrams: addressing the challenge of five degrees of freedom, Mater. Today 38 (2020) 49–57.

[68] E. Alpaydin, Introduction to Machine Learning, 3rd ed., MIT Press, Cambridge, USA, 2014.

[69] T. Mukherjee, T. DebRoy, Printability of 316 stainless steel, Sci. Technol. Weld. Join. 24 (2019) 412–419.